Interface Engineering of Hematite with Nacre-like Catalytic Multilayers for Solar Water Oxidation

Yeongkyu Choi,[†,⊥] Dasom Jeon,[‡,⊥] Yuri Choi,[†] Dongseok Kim,[§] Nayeong Kim,[‡] Minsu Gu,[‡] Sanghyun Bae,[‡] Taemin Lee,[†] Hyun-Wook Lee,[‡] Byeong-Su Kim,*,[§] and Jungki Ryu*,[‡]

[†]Department of Chemistry, School of Natural Science, Ulsan National Institute of Science and Technology (UNIST), Ulsan 44919, Republic of Korea
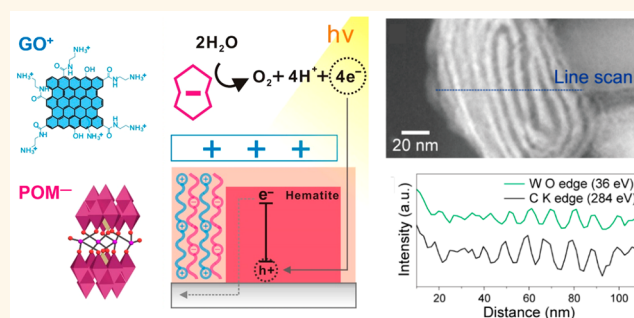
[‡]Department of Energy Engineering, School of Energy and Chemical Engineering, Ulsan National Institute of Science and Technology (UNIST), Ulsan 44919, Republic of Korea

[§]Department of Chemistry, Yonsei University, Seoul 03722, Republic of Korea

S Supporting Information

ABSTRACT: An efficient water oxidation photoanode based on hematite has been designed and fabricated by tailored assembly of graphene oxide (GO) nanosheets and cobalt polyoxometalate (Co-POM) water oxidation catalysts into a nacre-like multilayer architecture on a hematite photoanode. The deposition of catalytic multilayers provides a high photocatalytic efficiency and photo-electrochemical stability to underlying hematite photoanodes. Compared to the bare counterpart, the catalytic multilayer electrode exhibits a significantly higher photo-current density and large cathodic shift in onset potential (~369 mV) even at neutral pH conditions due to the improved charge transport and catalytic efficiency from the rational and precise assembly of GO and Co-POM. Unexpectedly, the polymeric base layer deposited prior to the catalytic multilayers improves the performance even more by facilitating the transfer of photogenerated holes for water oxidation through modification of the flat band potential of the underlying photoelectrode. This approach utilizing polymeric base and catalytic multilayers provides an insight into the design of highly efficient photoelectrodes and devices for artificial photosynthesis.

KEYWORDS: artificial photosynthesis, photocatalysis, graphene oxide, polyoxometalate, layer-by-layer assembly

Enabling efficient solar production of chemicals, so-called artificial photosynthesis, has long been considered as a promising solution for sustainable fuel and chemical production.[1−3] Based on the principles of natural photosynthesis,[4−7] studies on artificial photosynthesis have progressed from a fundamental understanding of the photophysical and photoelectrochemical (PEC) properties of semiconducting materials[8,9] to their practical application.[10−21] For example, various semiconducting materials, such as α-Fe$_2$O$_3$ (hematite),[8−15] Si,[15−17] and TiO$_2$[18−20] have been studied as a photoelectrode for hydrogen and/or oxygen evolution in a PEC cell. Especially, hematite is regarded as a promising photoanode for solar water oxidation due to its low cost, abundance, and wide visible-light absorption.[8−15] However, its intrinsic limitations, such as fast recombination (<10 ps), short hole diffusion length (2−4 nm), and high requisite over-potential (0.5−0.8 V), hinder the high efficiency and long-term stability, which become critical for practical application. To alleviate these limitations, diverse forms of photoelectrodes have been presented using various functional components, such as water oxidation catalysts (WOCs)[8−11] and charge-transporting materials.[18] Although these attempts have been effective, the importance of tailored assembly and precise interface engineering[22] has often not been a subject of intensive research to improve the photocatalytic performance even further.

Nature has developed its own strategy to build delicate and complicated biological systems through the rational design and precise assembly of multiple components.[4−7] Representative examples include the formation of photosynthetic machinery that efficiently produces biological fuels using sunlight in a

Scheme 1. Schematic Representation of LbL-Assembled $(GO/Co\text{-}POM)_n$ Multilayers on a Hematite Electrode with a Simplified Charge Transfer Pathway
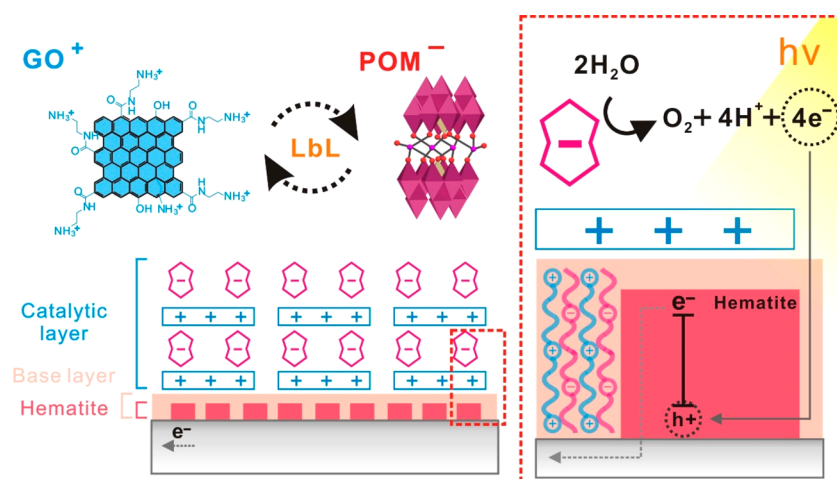
thylakoid membrane and mollusk shells having excellent mechanical properties. The precise molecular arrangement of light-harvesting pigments, redox-active molecules, and catalytic active sites in photosynthetic machinery ensures efficient harvesting of sunlight and directional transfer of electrons through machinery, resulting in the superior efficiency of natural photosynthesis.[4−7] Similarly, nacre has a delicate lamellar structure, where inorganic calcium carbonate crystals and organic polypeptides are hybridized with nanoscale precision.[23]

Inspired by such biological systems, we recently reported the fabrication of modular PEC devices using a layer-by-layer (LbL) method, which has been utilized for the fabrication of nacre-like structures.[14,24−30] The LbL method enabled the precise assembly of molecular WOCs and polyelectrolytes on various photoanode surfaces into an architecture reminiscent of the photosynthetic machinery with a significantly improved PEC performance, regardless of the type of underlying photoanodes.[14,26] Considering its simplicity, flexibility, and universal applicability,[14,24−26] the LbL method can be further utilized to design and fabricate various PEC devices assembled from multiple functional components. However, our previous studies have been limited to the proof-of-concept demonstration—assembly of a single functional component (i.e., WOCs) and its effect on performance improvement—and did not explore the potential role of polyelectrolytes in interface engineering.

In this study, we demonstrate the LbL approach of organic/inorganic hybrid photoanodes for efficient solar water oxidation through tailored assembly of multiple functional components and precise interface engineering with polyelectrolytes. Specifically, we have modified hematite with graphene oxide (GO) nanosheets and cobalt-based polyoxometalate $([Co_4(H_2O)_2(PW_9O_{34})_2]^{10-}$, Co-POM) for effective charge transport[31−34] and fast water oxidation electrocatalysis,[14,35] respectively. The tailored assembly of GO and Co-POM into nacre-like catalytic multilayers led to a synergistic enhancement in water oxidation performance. Interestingly, the predeposition of polymeric base layers improved the performance even more significantly by improving interfacial charge transport through tuning of flat band potential of the underlying electrode. We anticipate that this study will provide

a platform to assemble various nanoscale components to design high-performance multiscale hybrid PEC devices.

RESULTS AND DISCUSSION

The catalytic multilayers of GO and Co-POM (hereafter, $(GO/Co\text{-}POM)_n$, n denotes the number of bilayers (BL)) were fabricated on the hematite electrode by sequential deposition of cationic GO and anionic Co-POM exploiting the electrostatic interactions for solar water oxidation (Scheme 1). It is expected that GO and Co-POM can contribute to improved photoanode performance by facilitating selective and efficient transport of holes and catalytic extraction of electrons from water, respectively. Cationic GO was synthesized by covalently introducing amine groups on chemically exfoliated GO nanosheets.[36,37] In parallel, anionic Co-POM with a biomimetic oxo-bridged tetracobalt active site was prepared based on previous work.[35] These two suspensions exhibited considerable surface charges at the assembly conditions, as indicated by the zeta-potential measurement (Figure S1). Prior to the multilayer assembly, a polymeric base layer composed of three BL of poly(ethylene imine) (PEI) and poly(acrylic acid) (PAA) (i.e., $(PEI/PAA)_3$) was deposited to improve the coverage and uniformity of the multilayer film on the hematite electrode. The critical role of the base layer in tuning the flat band potential of the hematite electrode will be described more in the following discussion.

The successful assembly of $(GO/Co\text{-}POM)_n$ multilayer films was confirmed by scanning electron microscopy (SEM), UV/vis spectroscopy, ellipsometry, and quartz crystal microbalance (QCM) analysis (Figure S2). SEM images showed a significant morphological change to the hematite electrode after the assembly. While bare hematite has a worm-like structure, the deposition of the multilayers led to the formation of a sheet-like structure on its surface, a characteristics of GO nanosheets, resulting in a decrease in surface roughness (Figure S2a,b). In particular, the deposition of uniform and transparent films was clearly demonstrated through the linear growth of the characteristic absorption peak of GO at 230 nm (Figure S2c,d). Notably, the transmittance of the 17 BL films reached 93.5% at 400 nm, demonstrating that the catalytic multilayer had a negligible effect on the passage of light to the hematite electrode. Ellipsometry measurements also indicated a uniform increase in the thickness with an average BL
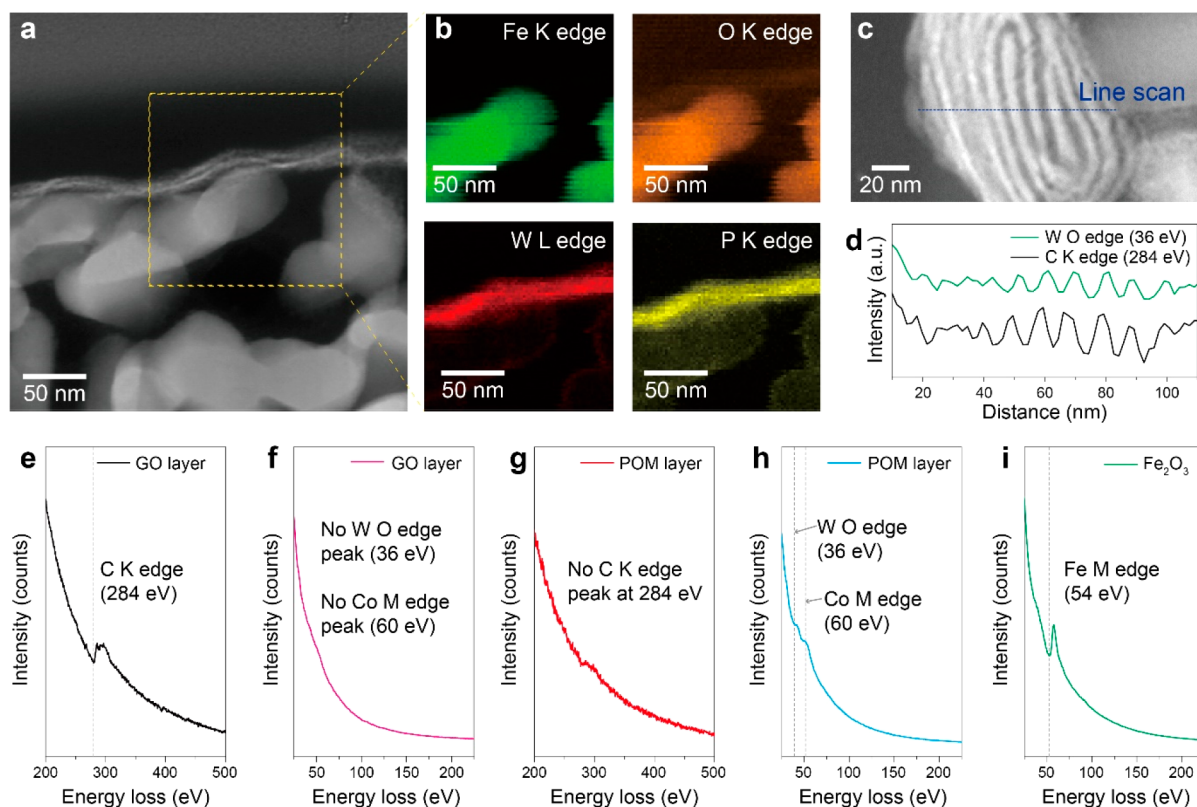
Figure 1. STEM characterization of the $(GO/Co\text{-}POM)_9$ multilayer films. (a) Cross-sectional STEM image and (b) EDS elemental mapping images of the $(GO/Co\text{-}POM)_9$ multilayer films on hematite. (c) High-magnification STEM image and (d) EELS line scan analysis of the $(GO/Co\text{-}POM)_{10}$ multilayer films. The green and black lines correspond to the intensity profile of W O edge and C K edge peaks, respectively. (e−i) Extracted EELS data on different positions of the multilayer: (e−h) C K, Co M, and W O edge spectra on (e, f) a GO layer and (g, h) a Co-POM layer and (i) Fe M edge spectra on the hematite electrode.

thickness of 0.61 ± 0.05 nm (Figure S2e). Independently, *in situ* QCM analysis quantitatively supported a linear growth in the $(GO/Co\text{-}POM)_n$ multilayer film (Figure S2f). For example, GO and Co-POM were deposited at a density of 0.25 and 0.41 $\mu g\ cm^{-2}$, respectively, in a single bilayer with a mass ratio of 1:1.6 (GO *vs* Co-POM). The consistent growth throughout the multilayer supported a uniform deposition of each functional component, such as GO and Co-POM, on top of the electrode.

To identify the precise nanoscale architecture of the $(GO/Co\text{-}POM)_n$ multilayer film assembled on the hematite electrode, we carried out cross-sectional scanning transmission electron microscopy (STEM), energy-dispersive X-ray spectroscopy (EDS), and electron energy loss spectroscopy (EELS) analyses. The STEM (Figure 1a and Figure S3) and EDS elemental mapping analyses indicated that the hybrid multilayers of $(GO/Co\text{-}POM)_n$ with W and P elements of POM were deposited evenly on the ragged and worm-like hematite electrode with Fe and O elements (Figure 1b). The high-magnification STEM image shows the alternating multilayer film by the clear contrast difference: dark Co-POM layers, with heavy elements such as W and Co, along with bright GO layers, with elements such as C and O (Figure 1c). The corresponding EELS analysis clearly distinguished the alternating GO and Co-POM layers within the multilayer film (Figure 1d). Accordingly, the chemical contents varied with respect to position, highlighting the sequential deposition of the corresponding components. Specifically, the peaks on the C K edge (284 eV) and the W O edge (36 eV) were

displayed as alternating, with a clear contrast difference in a distance span of approximately 4 nm (Figure 1c,d). Only the C K peak was clearly observed in the GO layer (Figure 1e,f), and the W O and Co P peaks were observed in the Co-POM layer (Figure 1g,h). In addition, the peak at 54 eV corresponded to the Fe M edge in the hematite electrode (Figure 1i). Unlike the polymeric base layers, which were difficult to identify due to the low contrast and interpenetration of polymer chains, the $(GO/Co\text{-}POM)_9$ film clearly exhibited alternating nanoscale multilayers of organic and inorganic components albeit with a large structural difference in the two-dimensional GO and zero-dimensional Co-POM (hundreds of nm *vs* 1−2 nm in diameter). The observed thickness difference between STEM and ellipsometry (about 4 *vs* 0.61 ± 0.05 nm per BL) could have originated from differences in surface roughness of the hematite electrode for STEM and silicon wafer for ellipsometry.[38] On the basis of the detailed STEM and EELS characterization, we verified that the alternating deposition of GO and Co-POM using the simple LbL process led to the formation of a nacre-like hybrid film with nanoscale precision.

After confirming the successful growth of hybrid films of $(GO/Co\text{-}POM)_n$, they were subjected to thermal reduction to improve their PEC performance for water oxidation. It is well known that the thermal reduction of GO leads to an increase in its electrical conductivity, especially hole-transporting properties.[31,32] The nine BL films were selected as a representative sample and reduced at three different temperatures, 100, 200, and 300 °C. The efficiency of the samples was evaluated by linear sweep voltammetry (LSV) under light and
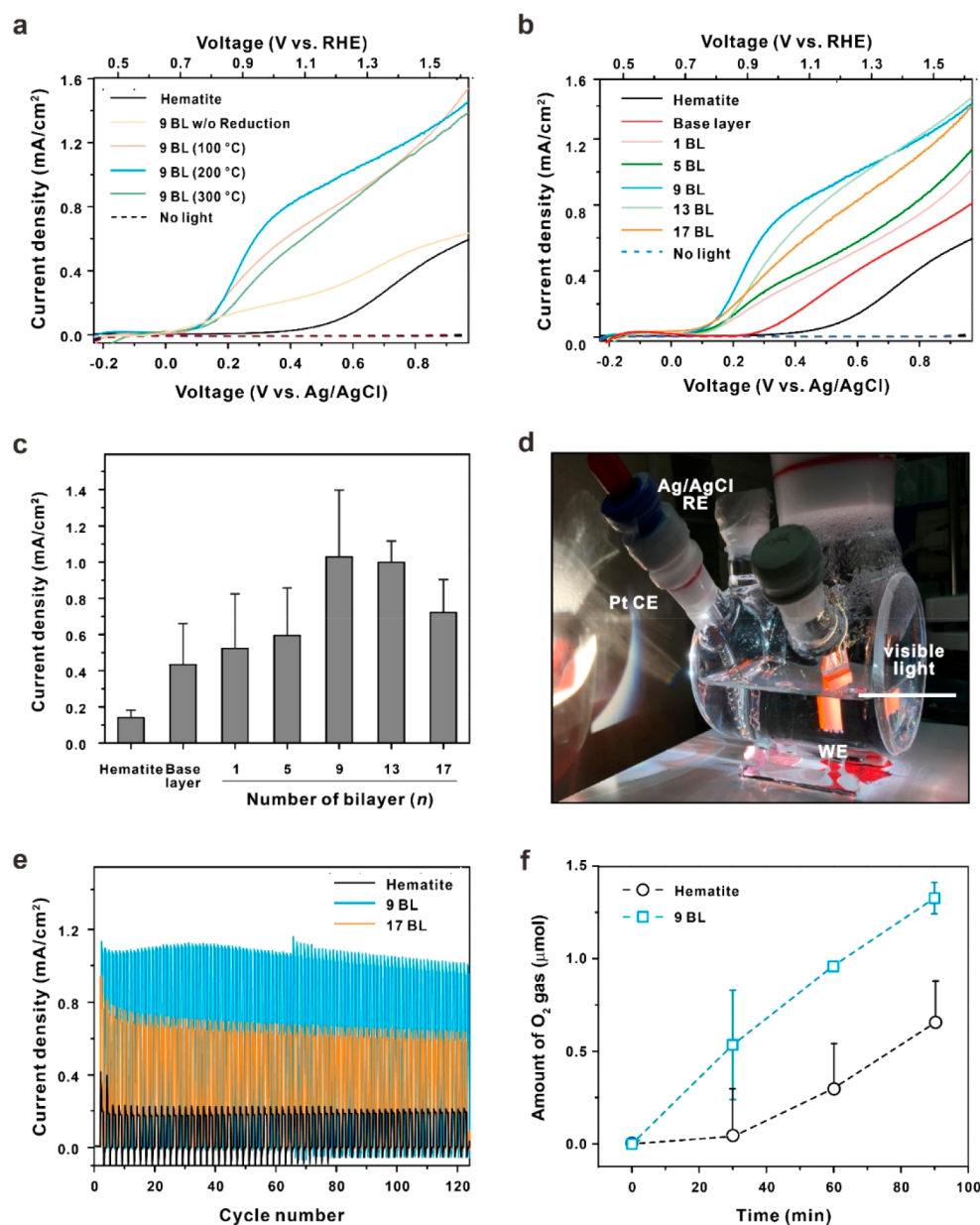
Figure 2. Photoelectrochemical performance of the hematite photoanode with the catalytic multilayers. (a) Effect of the thermal reduction of GO on the performance of the hematite photoanode with $(PEI/PAA)_3/(GO/Co-POM)_9$. (b, c) Influence of the number of catalytic layers (BL, *n*). (c) Comparison between performances of various photoanodes in terms of photocurrent density at 1.23 V *vs* RHE. (d) Photograph of experimental configuration for (e) long-term stability test for 3 h and (f) gas evolution analysis. (e) Cycling test showing the long-term stability of the catalytic multilayer films under the applied bias of 1.23 V *vs* RHE. (f) Time series of O_2 gas evolution by the hematite photoanode with $(PEI/PAA)_3/(GO/Co-POM)_9$ film under visible light irradiation.

dark conditions (Figure 2a). Even before reduction, the hematite photoanode with the hybrid film exhibited a significantly improved performance in terms of onset potential and photocurrent density, implying a catalytic effect of the hybrid film. Both X-ray photoelectron spectroscopy (XPS) and Raman spectroscopy confirmed the successful reduction of GO and preservation of elemental distribution after the reduction (Figure S4). The thermal reduction of GO had a negligible effect on the onset potential for water oxidation, but displayed a significant effect on the increase in photocurrent density of the hematite electrode, which can be attributed to the improved electrical properties of GO upon reduction. Note that onset potential values were determined as the value where dJ/dV is equal to 0.2 mA cm^{-2} V^{-1}, where J is the measured

photocurrent density and *V* is the applied bias, according to the literature.[13,39] The efficiency increased for samples treated from 100 to 200 °C and then decreased at 300 °C. For example, the photocurrent densities of hematite electrodes assembled with $(GO/Co-POM)_9$ were 0.49 (no treatment), 0.83 (100 °C), 1.03 (200 °C), and 0.78 mA cm^{-2} (300 °C), respectively, at pH 8.0 and an applied bias of 1.23 V *vs* reversible hydrogen electrode (RHE). We hypothesize that the dependence of the performance of the hematite photoanode on reduction temperature resulted from the compromise between the increased conductivity of the multilayer films and thermal degradation of the polymeric base layers upon thermal reduction. One can expect that the performance improvement results from the formation of oxygen vacancies upon
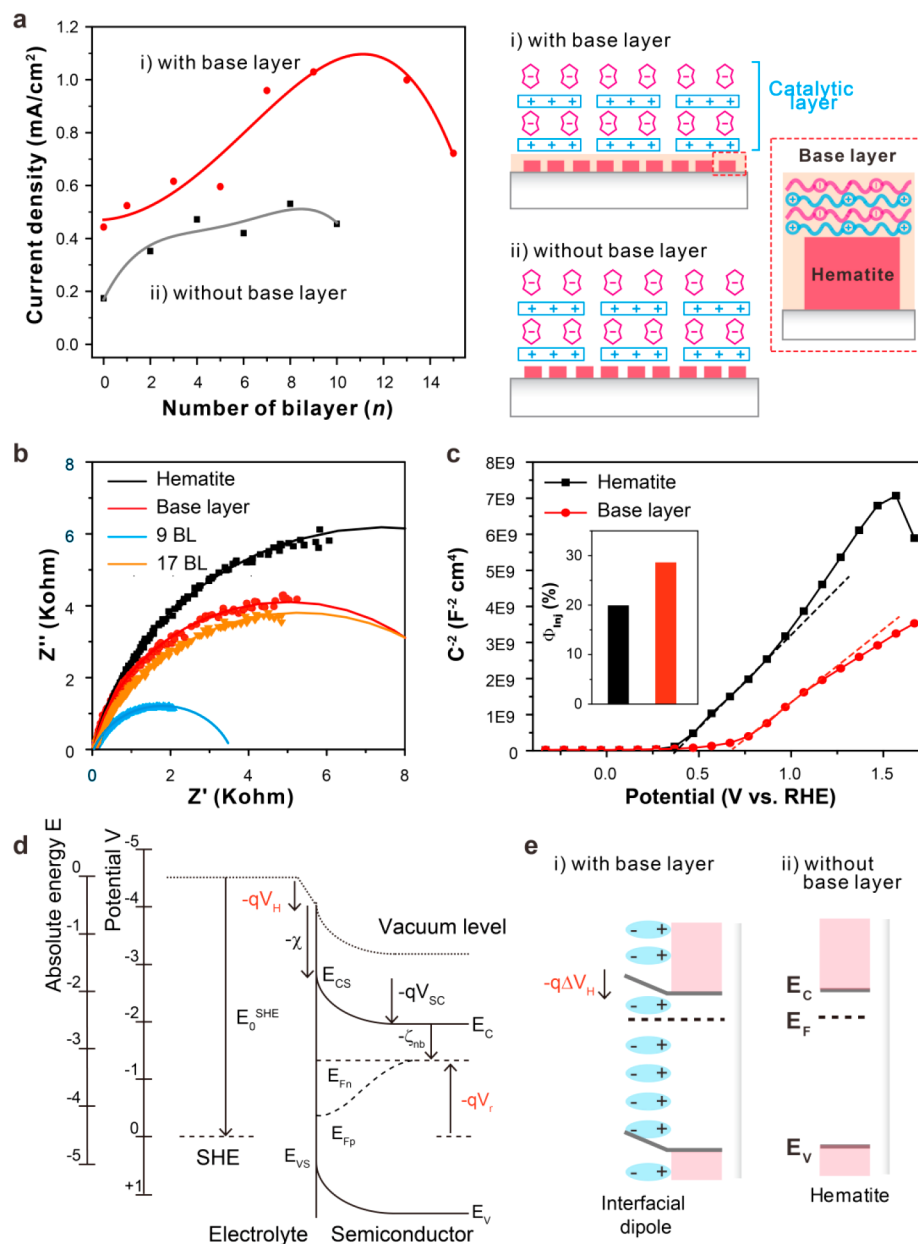
Figure 3. Role of the base and catalytic multilayers in the performance improvement of the hematite photoanode. (a) Effect of three BL of polymeric base layers on the performance of the hematite electrode with the catalytic multilayers. The solid lines are respective polynomial fitted curves. (b) Nyquist plots of impedance for hematite electrode with catalytic multilayers. (c) Mott−Schottky plots for the hematite photoanodes in the presence and absence of the polymeric base layers. Inset shows the charge injection efficiency for the corresponding photoanodes. (d) Energy level diagram showing the definition of various physical and electrochemical quantities. (e) Illustrations showing the effect of the interfacial dipole on the energy level of semiconductor photoanodes.

annealing.[40,41] XPS analysis revealed that large amounts of oxygen vacancies were formed even at a relatively low temperature of 200 °C under an Ar atmosphere with 4% H_2 (Figure S5). Considering the thickness of catalytic multilayers (*ca.* 20−30 nm) and surface-sensitive characteristics of XPS analysis, however, it is difficult to assert that oxygen vacancies were preferentially formed in hematite. Further studies are required to unveil the identity and role of oxygen vacancies in our system and will be reported in due course.

On the basis of these results, we optimized the conditions for the catalytic multilayer assembly, enabling efficient and stable solar water oxidation by the hematite photoanode. When we investigated the effect of the BL number (*i.e.*,

thickness) of the catalytic multilayers, we found that nine BL exhibited the best performance in terms of photocurrent density (Figure 2b,c and Figure S6). Although there was a negligible difference in the onset potential values between samples with a different number of catalytic multilayers (*n* ranges from 1 to 17 BL), there was a huge cathodic shift of 369 mV in the onset potential compared to the bare hematite (1.07 V *vs* RHE). To the best of our knowledge, it is one of the largest cathodic shifts in onset potential for the hematite photoanode, irrespective of measurement conditions such as pH, electrolyte concentration, and light intensity (see Table S1).[42] After the optimization, we further carried out the incident photon-to-current conversion efficiency (IPCE)

measurement to study the effect of the catalytic multilayers on the wavelength-dependent photochemical properties of the hematite photoanodes (Figure S7). Except for a significant increase in the efficiency after the deposition of the catalytic multilayers, the IPCE and absorbance spectra of both photoanodes (bare and nine BL) exhibited a similar wavelength-dependent response, confirming the negligible effect of the catalytic multilayers on the photogeneration of charge carriers. As a control, we further modified the hematite photoanode with GO alone, Co-POM alone, or randomly mixed GO and Co-POM by drop-casting in the absence of the base layer. In these control experiments, the amount of each component deposited and their relative ratio were kept identical to those in the LbL assembly. As shown in Figure S8, there was a negligible or even detrimental effect on the performance of the hematite photoanode when modified by drop-casting, regardless of the type of deposited materials. These results clearly demonstrate the importance of tailored nanoscale assembly of functional components to improve the performance of the underlying photoelectrode.

Next, we performed a chronoamperometric cycling test to evaluate the stability of our catalytic multilayers on the hematite electrode upon PEC water oxidation (Figure 2d,e). As shown in Figure 2e, the hematite electrode with our catalytic multilayers exhibited a much higher photocurrent density compared to the bare counterpart. It is noteworthy here that, unlike other samples, the $(GO/Co-POM)_9$ sample occasionally led to a gradual and abrupt increase in photocurrent density during the measurement. Considering that such a phenomenon is frequently observed due to the formation and detachment of gas bubbles in the active electrode,[43] we attribute these changes to a higher catalytic efficiency of the $(GO/Co-POM)_9$ film. To further verify that the $(GO/Co-POM)_n$ multilayers on the hematite photoanode were indeed generating oxygen gas during the solar water oxidation without unwanted side reactions, gas chromatography (GC) was used to measure the amount of evolved gases under continuous visible light illumination (Figure 2f). Interestingly, the amount of evolved oxygen gas from the $(GO/Co-POM)_9$ hybrid film was 2 to 3 times higher than the bare hematite electrode. The Faradaic efficiency of the hematite photoanode without and with catalytic multilayers was 57.6% and 84.6%, respectively. The slight deviation from the ideal efficiency of 100% can be attributed to photocorrosion of hematite at neutral pH.[10] The turnover frequency of Co-POM was 1.88×10^3 h^{-1} for the hematite electrode assembled with the base and catalytic layers of $(PEI/PAA)_3/(GO/Co-POM)_9$. Taken together, these results confirm a higher efficiency and stability of the catalytic multilayers.

During optimization, the unexpected role of the polymeric base layer was unveiled and found to contribute to the performance improvement of the hematite photoanode. Initially, the base layer was introduced prior to the assembly of the catalytic multilayers of $(GO/Co-POM)_n$ to improve their adhesion to the hematite photoanode. Interestingly, the deposition of the base layer alone resulted in the increase of the photocurrent density and a slight cathodic shift ($\sim$182 mV) of onset potential (Figure 2b). Encouraged by these findings, we systematically investigated the relationship between the number of polymeric base layers, number of the catalytic multilayers, and the performance of the hematite photoanode in terms of photocurrent density. The predeposition of the base layer significantly improved the PEC water

oxidation performance (Figure 3a). For example, the hematite photoanodes exhibited the best performance when both the three BL of the base layer and nine BL of the catalytic multilayer were deposited together. For the hematite with nine BL of the catalytic multilayers, the current densities were 1.03 and 0.51 mA cm^{-2} at 1.23 V vs RHE with and without three BL of the base layer, respectively. To elucidate the underlying mechanism for the improvement, the electrochemical impedance spectra (EIS) were evaluated (Figure 3b). The EIS of the hematite electrode with the base layer $(PEI/PAA)_3$ alone exhibited a smaller resistance for both charge transport in the hematite electrode (R_1) and electrocatalytic charge transfer (R_2) compared to the bare counterpart (see Table S2). Further deposition of the catalytic multilayers led to an even more significant decrease, demonstrating the respective role of GO and Co-POM as an efficient charge-transporting material and effective WOC as stated earlier. We hypothesize that the base layers contribute to the improvement by affecting flat band potential of the hematite photoanode with its dipole moment and tuning the band-edge position more favorable for overall water splitting.

To support our hypothesis on the interfacial dipole effect of the polymeric base layers, the flat band potentials (V_{fb}) of the hematite photoanode with and without the base layers were determined using Mott−Schottky (M-S) analysis (Figure 3c). According to literature,[44] the flat band potential (V_{fb}) can be determined by the expression $V_{fb} = \frac{E_0^{SHE} + \chi + \zeta_{nb}}{q} + V_H^{fb}$ where E_0^{SHE} is the energy of standard hydrogen electrode (SHE) with respect to the vacuum level of the electron (−4.44 eV), χ is the electron affinity for hematite, ζ_{nb} is the difference between the energy of the conduction band edge and the electron Fermi level, and V_H^{fb} is the potential drop across the Helmholtz layer due to the presence of adsorbed ions and dipoles under flat band conditions (Figure 3d). The deposition of polymeric base layers resulted in a large shift of the flat band potential of about 200 mV. On the contrary, there was a negligible change in the slope of the M-S plot and thus the charge carrier density in the hematite photoanode, implying that χ and ζ_{nb} are constant for both samples. Thus, the observed difference in the flat band potentials can be attributed to different V_H^{fb} values, suggesting the presence of a local dipole moment originating from the alternating layers of cationic and anionic materials (Figure 3e). After the deposition of the base layer, interestingly, the shift of onset potential was comparable to that of the flat band potential ($\sim$200 mV), while the charge injection efficiency was considerably improved (Figure 3c inset), supporting our hypothesis that the local dipole moment formed by the deposition of a polymeric base layer improved the charge separation and injection efficiency. Our finding is consistent with recent reports on the fabrication of a low work-function electrode by the deposition of polyelectrolytes.[45−47] Further study is currently underway to disclose its underling mechanism more clearly. This study is noteworthy in that GO, Co-POM, and polymeric base layers are rationally assembled on hematite considering the energy level of each material and effective charge transfer. GO as a hole-transporting material offers a conductive basement and Co-POM acts as a WOC, respectively. In addition, the polymeric base layer effectively tuned the flat band potential for enhanced catalytic dipole development. Finally, it is significant that all electrode assembly is performed in an aqueous solution, which

could offer potential in an environmentally friendly and universally applicable protocol for future electrode engineering.

CONCLUSIONS

In summary, we developed catalytic multilayers that integrate GO and Co-POM by layer-by-layer assembly to improve the artificial photosynthetic efficiency of a hematite electrode. This catalytic multilayer was precisely optimized with the amount of catalysts by adjusting the number of catalytic multilayers and additional heat treatment for high photocatalytic efficiency. The hematite electrode assembled with organic and inorganic hybrid multilayers showed a superior photocatalytic activity compared with a bare hematite electrode, indicating that the catalytic multilayers play an important role in the effective hole transfer to water. Moreover, the polyelectrolyte base layer offered a crucial influence on photocatalytic performance through the tuning of surface dipole and flat band potential for efficient charge separation and injection. We anticipate that this study will provide a platform for designing and developing a high-performance artificial photosynthetic photoanode.

METHODS

Synthesis. Graphene oxide was prepared using a modified Hummer's method and functionalized with an amine group through covalent coupling with ethylene diamine in the presence of 1-[3-(dimethylamino)propyl]-3-ethylcarbodiimide methiodide.[36,37] Cobalt polyoxometalate, $[Co_4(H_2O)_2(PW_9O_{34})_2]^{10-}$, was synthesized according to the literature.[35] The hematite photoanode was hydrothermally grown on a fluorine-doped tin oxide (FTO) substrate according to the method described by Jang et al.[15]

Deposition of Polymeric Base Layers and Catalytic (GO/Co-POM)$_n$ Layers. Poly(ethylene imine) (Polymer Science; M_w 10 000) and poly(acrylic acid) solutions (Sigma-Aldrich; M_w 250 000) were prepared as 5 mg mL^{-1} as cationic and anionic polyelectrolyte solutions, respectively, for deposition of the base layers. In the case of the deposition of the catalytic (GO/Co-POM)$_n$ layers, GO and Co-POM solutions were prepared at concentrations of 0.50 mg mL^{-1} and 1.0 mM as cationic and anionic components, respectively. Prior to LbL assembly, substrates were treated with oxygen plasma to increase their hydrophilicity and the solution pH was adjusted to 6.0. (PEI/PAA)$_n$ base layers and subsequent (GO/Co-POM)$_n$ catalytic layers were deposited using an automatic dip-spin coater (Strato Sequence IV) in the following order for the described number of times: cationic PEI (or GO) solution for 10 min (or 3 min), deionized (DI) water three times for 1 min each to remove any unbound polymer, anionic PAA (or Co-POM) solution for 10 min (or 3 min), and DI water three times for 1 min each. The assembled (GO/Co-POM)$_n$ multilayer films were thermally reduced in a tube furnace (Thermal CVD for graphene, Cyntec Co.) under the following condition: heating rate of 10 °C per min, annealing temperature of 100, 200, or 300 °C, and Ar atmosphere containing 4% H$_2$.

Characterizations. The surface ζ-potential of GO and Co-POM was measured to confirm the LbL condition using a ζ-potential analyzer (Malvern, Zetasizer Nano ZS). The absorbance of (GO/Co-POM)$_n$ multilayers on a quartz substrate was characterized by UV−vis spectroscopy (Cary 5000, Varian). The film thicknesses on the silicon substrate were measured by ellipsometry (J. A. Woollam Co. Inc., EC-400 and M-2000V). The loading mass of each material absorbed onto the film surface was analyzed by a quartz crystal microbalance (Stanford Research System, QCM200), according to the literature.[38] The LbL films were analyzed by XPS (Thermo Fisher, ESCALAB 250XI). The reduction state of GO was confirmed by Raman spectroscopy (Witec, Alpha300). Structural investigation including SEM, STEM images, EDS mapping, and EELS of the (GO/Co-POM)$_n$ multilayer films was conducted using a Nova nanoSEM (FEI) and a JEM-2100F high-resolution transmission electron microscope (JEOL). Samples for STEM analysis were prepared using a dual-beam focused ion beam (FEI, Quanta 3D FEG). The energy resolution of the EELS spectrometer is about 0.9 eV as measured by the full width at half-magnitude of the zero-loss peak. The energy window of the EELS was 25−225 eV for W (W O edge, 36 eV), Co (Co M edge, 60 eV), and Fe (Fe M edge 54 eV) peaks and 170−570 eV for the C (C K edge, 284 eV) peak.

Photoelectrochemical Characterizations. All photoelectrochemical characterizations were conducted in 80 mM phosphate buffer (pH 8.0). The performance of the hematite-based photoanodes was evaluated by measurement with an LSV under visible light illumination (100 mW cm^{-2}) with a WMPG1000 multichannel potentiostat/galvanostat under the following conditions: Ag/AgCl reference electrode, Pt planar counter electrode, and 20 mV s^{-1} scan rate. A 300 W Xe lamp equipped with a 400 nm cut-on filter was used as a visible light source. Evolved oxygen and hydrogen gases during the PEC test were quantified with a GC-2010 Plus gas chromatograph (Shimadzu Co., Japan). Electrochemical impedance spectra were measured using a 1260 impedance analyzer (Solartron) under the following conditions: Ag/AgCl reference electrode, Pt wire counter electrode, 0.5 V applied potential, 10 mV amplitude, and 100 kHz to 0.1 Hz frequency scan range. Mott−Schottky analysis was carried out using a CP-150 potentiostat/galvanostat (Bio-Logic Science Instruments, France) under the following conditions: Ag/AgCl reference electrode, Pt counter electrode, and frequency of 1000 Hz. The charge injection efficiency was determined by comparing photocurrent densities at 1.23 V vs RHE in the presence and absence of Na$_2$SO$_3$ as a hole scavenger.

ASSOCIATED CONTENT

Ⓢ Supporting Information

The Supporting Information is available free of charge on the ACS Publications website at DOI: 10.1021/acsnano.8b06848.

pH-dependent ζ-potentials of assembling components; SEM and TEM images of the catalytic multilayers; UV/vis absorbance spectroscopy, ellipsometry, and QCM analysis of the catalytic multilayers; XPS and Raman spectra showing the thermal reduction of GO; photocurrent profiles of the hematite photoanodes with the catalytic multilayers under periodic illumination; performance comparison of various hematite-based photoanodes in recent literature; IPCE spectra of the hematite photoanodes with and without the catalytic multilayers; comparison between the performance of hematite photoanode with and without modification with Co-POM and GO by various methods; the effect of polymeric base layer on the performance of the hematite electrode; the fitting results of Nyquist plot (PDF)

AUTHOR INFORMATION

Corresponding Authors
*E-mail: bskim19@yonsei.ac.kr.
*E-mail: jryu@unist.ac.kr.
ORCID ⓘ
Yeongkyu Choi: 0000-0001-5680-1390
Dasom Jeon: 0000-0002-2297-0396
Yuri Choi: 0000-0002-4691-230X
Nayeong Kim: 0000-0002-8173-1889
Minsu Gu: 0000-0002-6270-7496
Sanghyun Bae: 0000-0002-6108-2324
Hyun-Wook Lee: 0000-0001-9074-1619
Byeong-Su Kim: 0000-0002-6419-3054
Jungki Ryu: 0000-0002-0897-8463
Author Contributions
[1]Y. Choi and D. Jeon contributed equally to this work.

REFERENCES

(1) Nocera, D. G. The Artificial Leaf. *Acc. Chem. Res.* **2012**, *45*, 767−776.

(2) Walter, M. G.; Warren, E. L.; McKone, J. R.; Boettcher, S. W.; Mi, Q.; Santori, E. A.; Lewis, N. S. Solar Water Splitting Cells. *Chem. Rev.* **2010**, *110*, 6446−6473.

(3) Kim, D.; Sakimoto, K. K.; Hong, D.; Yang, P. Artificial Photosynthesis for Sustainable Fuel and Chemical Production. *Angew. Chem., Int. Ed.* **2015**, *54*, 3259−3266.

(4) Ferreira, K. N. Architecture of the Photosynthetic Oxygen-Evolving Center. *Science* **2004**, *303*, 1831−1838.

(5) Renger, G.; Renger, T. Photosystem II: The Machinery of Photosynthetic Water Splitting. *Photosynth. Res.* **2008**, *98*, 53−80.

(6) Lubitz, W.; Reijerse, E. J.; Messinger, J. Solar Water-Splitting into H_2 and O_2: Design Principles of Photosystem II and Hydrogenases. *Energy Environ. Sci.* **2008**, *1*, 15−31.

(7) McEvoy, J. P.; Brudvig, G. W. Water-Splitting Chemistry of Photosystem II. *Chem. Rev.* **2006**, *106*, 4455−4483.

(8) Carroll, G. M.; Zhong, D. K.; Gamelin, D. R. Mechanistic Insights into Solar Water Oxidation by Cobalt-Phosphate-Modified α-Fe_2O_3 Photoanodes. *Energy Environ. Sci.* **2015**, *8*, 577−584.

(9) Carroll, G. M.; Gamelin, D. R. Kinetic Analysis of Photoelectrochemical Water Oxidation by Mesostructured Co-Pi/α-Fe_2O_3 Photoanodes. *J. Mater. Chem. A* **2016**, *4*, 2986−2994.

(10) Kim, J. Y.; Jang, J. W.; Youn, D. H.; Magesh, G.; Lee, J. S. A stable and Efficient Hematite Photoanode in a Neutral Electrolyte for Solar Water Splitting: Towards Stability Engineering. *Adv. Energy Mater.* **2014**, *4*, 1400476.

(11) Tamirat, A. G.; Rick, J.; Dubale, A. A.; Su, W.-N.; Hwang, B.-J. Using Hematite for Photoelectrochemical Water Splitting: A Review of Current Progress and Challenges. *Nanoscale Horiz* **2016**, *1*, 243−267.

(12) Hisatomi, T.; Dotan, H.; Stefik, M.; Sivula, K.; Rothschild, A.; Gratzel, M.; Mathews, N. Enhancement in the Performance of Ultrathin Hematite Photoanode for Water Splitting by an Oxide Underlayer. *Adv. Mater.* **2012**, *24*, 2699−2702.

(13) Le Formal, F.; Grätzel, M.; Sivula, K. Controlling Photoactivity in Ultrathin Hematite Films for Solar Water-Splitting. *Adv. Funct. Mater.* **2010**, *20*, 1099−1107.

(14) Jeon, D.; Kim, H.; Lee, C.; Han, Y.; Gu, M.; Kim, B.-S.; Ryu, J. Layer-by-Layer Assembly of Polyoxometalates for Photoelectrochemical (PEC) Water Splitting: Toward Modular PEC Devices. *ACS Appl. Mater. Interfaces* **2017**, *9*, 40151−40161.

(15) Jang, J. W.; Du, C.; Ye, Y.; Lin, Y.; Yao, X.; Thorne, J.; Liu, E.; McMahon, G.; Zhu, J.; Javey, A.; Guo, J.; Wang, D. Enabling Unassisted Soar Water Splitting by Iron Oxide and Silicon. *Nat. Commun.* **2015**, *6*, 7447.

(16) Lee, H. Y.; Ryu, J.; Kim, J. H.; Lee, S. H.; Park, C. B. Biocatalyzed Artificial Photosynthesis by Hydrogen-Terminated Silicon Nanowires. *ChemSusChem* **2012**, *5*, 2129−2132.

(17) Shi, Y. Y.; Gimbert-Surinach, C.; Han, T. T.; Berardi, S.; Lanza, M.; Llobet, A. CuO-Functionalized Silicon Photoanodes for Photoelectrochemical Water Splitting Devices. *ACS Appl. Mater. Interfaces* **2016**, *8*, 696−702.

(18) Ryu, J.; Lee, S. H.; Nam, D. H.; Park, C. B. Rational Design and Engineering of Quantum-Dot-Sensitized TiO_2 Nanotube Arrays for Artificial Photosynthesis. *Adv. Mater.* **2011**, *23*, 1883−1888.

(19) Raja, R.; Sudhagar, P.; Devadoss, A.; Terashima, C.; Shrestha, L. K.; Nakata, K.; Jayavel, R.; Ariga, K.; Fujishima, A. Pt-Free Solar Driven Photoelectrochemical Hydrogen Fuel Generation using 1T MoS_2 Co-catalyst Assembled CdS QDs/TiO_2 photoelectrode. *Chem. Commun.* **2015**, *51*, 522−525.

(20) Valenti, G.; Boni, A.; Melchionna, M.; Cargnello, M.; Nasi, L.; Bertoni, G.; Gorte, R. J.; Marcaccio, M.; Rapino, S.; Bonchio, M.; Fornasiero, P.; Prato, M.; Paolucci, F. Co-axial Heterostructures Integrating Palladium/Titanium Dioxide with Carbon Nanotubes for Efficient Electrocatalytic Hydrogen Evolution. *Nat. Commun.* **2016**, *7*, 13549.

(21) Maeda, K.; Domen, K. Development of Novel Photocatalyst and Cocatalyst Materials for Water Splitting under Visible Light. *Bull. Chem. Soc. Jpn.* **2016**, *89*, 627−648.

(22) Jiang, C.; Moniz, S. J. A.; Wang, A.; Zhang, T.; Tang, J. Photoelectrochemical Devices for Solar Water Splitting − Materials and Challenges. *Chem. Soc. Rev.* **2017**, *46*, 4645−4660.

(23) Barthelat, F. Nacre from Mollusk Shells: A Model for High-Performance Structural Materials. *Bioinspiration Biomimetics* **2010**, *5*, 035001.

(24) Zakaria, M. B.; Li, C.; Ji, Q.; Jiang, B.; Tominaka, S.; Ide, Y.; Hill, J. P.; Ariga, K.; Yamauchi, Y. Self-Construction from 2D to 3D: One-Pot Layer-by-Layer Assembly of Graphene Oxide Sheets Held Together by Coordination Polymers. *Angew. Chem., Int. Ed.* **2016**, *55*, 8426−8430.

(25) Zhao, Y.; Li, W.; Jiang, X.; Li, F.; Li, X.; Zhang, W.; Jiang, J. S.; Liu, J.; Ariga, K.; Hu, M. Coordination Polymer Nanoglue: Robust Adhesion Based on Collective Lamellar Stacking of Nanoplates. *ACS Nano* **2017**, *11*, 3662−3670.

(26) Kim, H.; Bae, S.; Jeon, D.; Ryu, J. Fully Solution-Processable Cu_2O−$BiVO_4$ Photoelectrochemical Cells for Bias-Free Solar Water Splitting. *Green Chem.* **2018**, *20*, 3732−3742.

(27) Yeom, B.; Sain, T.; Lacevic, N.; Bukharina, D.; Cha, S.-H.; Waas, A. M.; Arruda, E. M.; Kotov, N. A. Abiotic Tooth Enamel. *Nature* **2017**, *543*, 95−98.

(28) Wan, S.; Peng, J.; Li, Y.; Hu, H.; Jiang, L.; Cheng, Q. Use of Synergistic Interactions to Fabricate Strong, Tough, and Conductive Artificial Nacre Based on Graphene Oxide and Chitosan. *ACS Nano* **2015**, *9*, 9830−9836.

(29) Yao, H. B.; Tan, Z. H.; Fang, H. Y.; Yu, S. H. Artificial Nacre-like Bionanocomposite Films from the Self-Assembly of Chitosan-Montmorillonite Hybrid Building Blocks. *Angew. Chem., Int. Ed.* **2010**, *49*, 10127−10131.

(30) Yan, L.; Chang, Y. N.; Yin, W.; Tian, G.; Zhou, L.; Hu, Z.; Xing, G.; Gu, Z.; Zhao, Y. Enhanced Multifunctional Properties of Graphene Nanocomposites with Nacre-like Structures. *Adv. Eng. Mater.* **2015**, *17*, 523−531.

(31) Jung, I.; Dikin, D. A.; Piner, R. D.; Ruoff, R. S. Tunable Electrical Conductivity of Individual Graphene Oxide Sheets Reduced at "Low" Temperatures. *Nano Lett.* **2008**, *8*, 4283−4287.

(32) Lee, D. W.; Hong, T. K.; Kang, D.; Lee, J.; Heo, M.; Kim, J. Y.; Kim, B. S.; Shin, H. S. Highly Controllable Transparent and Conducting Thin Films using Layer-by-Layer Assembly of Oppositely Charged Reduced Graphene Oxides. *J. Mater. Chem.* **2011**, *21*, 3438−3442.

(33) Kwon, S. R.; Harris, J.; Zhou, T. Y.; Loufakis, D.; Boyd, J. G.; Lutkenhaus, J. L. Mechanically Strong Graphene/Aramid Nanofiber Composite Electrodes for Structural Energy and Power. *ACS Nano* **2017**, *11*, 6682−6690.

(34) Li, Q.; Li, X.; Wageh, S.; Al-Ghamdi, A. A.; Yu, J. G. CdS/Graphene Nanocomposite Photocatalysts. *Adv. Energy Mater.* **2015**, *5*, 1500010.

(35) Yin, Q.; Tan, J. M.; Besson, C.; Geletii, Y. V.; Musaev, D. G.; Kuznetsov, A. E.; Luo, Z.; Hardcastle, K. I.; Hill, C. L. A Fast Soluble

Carbon-Free Molecular Water Oxidation Catalyst Based on Abundant Metals. *Science* **2010**, *328*, 342−345.

(36) Ahn, E.; Lee, T.; Gu, M.; Park, M.; Min, S. H.; Kim, B.-S. Layer-by-Layer Assembly for Graphene-Based Multilayer Nanocomposites: The Field Manual. *Chem. Mater.* **2017**, *29*, 69−79.

(37) Bao, H.; Pan, Y.; Ping, Y.; Sahoo, N. G.; Wu, T.; Li, L.; Li, J.; Gan, L. H. Chitosan-Functionalized Graphene Oxide as a Nanocarrier for Drug and Gene Delivery. *Small* **2011**, *7*, 1569−1578.

(38) Ahn, E.; Kim, B.-S. Multidimensional Thin Film Hybrid Electrodes with MoS_2 Multilayer for Electrocatalytic Hydrogen Evolution Reaction. *ACS Appl. Mater. Interfaces* **2017**, *9*, 8688−8695.

(39) Du, C.; Yang, X. G.; Mayer, M. T.; Hoyt, H.; Xie, J.; McMahon, G.; Bischoping, G.; Wang, D. W. Hematite-Based Water Splitting with Low Turn-On Voltages. *Angew. Chem., Int. Ed.* **2013**, *52*, 12692−12695.

(40) Jozwiak, W. K.; Kaczmarek, E.; Maniecki, T. P.; Ignaczak, W.; Maniukiewicz, W. Reduction Behavior of Iron Oxides in Hydrogen and Carbon Monoxide Atmospheres. *Appl. Catal., A* **2007**, *326*, 17−27.

(41) Ling, Y.; Wang, G.; Reddy, J.; Wang, C.; Zhang, J. Z.; Li, Y. The Influence of Oxygen Content on the Thermal Activation of Hematite Nanowires. *Angew. Chem., Int. Ed.* **2012**, *51*, 4074−4079.

(42) Li, H.; Liu, R.; Kong, W.; Liu, J.; Liu, Y.; Zhou, L.; Zhang, X.; Lee, S.-T.; Kang, Z. Carbon Quantum Dots with Photo-generated Proton Property as Efficient Visible Light Controlled Acid Catalyst. *Nanoscale* **2014**, *6*, 867−873.

(43) Clement, N.; Nishiguchi, K.; Dufreche, J. F.; Guerin, D.; Fujiwara, A.; Vuillaume, D. Water Electrolysis and Energy Harvesting with Zero-Dimensional Ion-Sensitive Field-Effect Transistors. *Nano Lett.* **2013**, *13*, 3903−3908.

(44) Bisquert, J.; Cendula, P.; Bertoluzzi, L.; Gimenez, S. Energy Diagram of Semiconductor/Electrolyte Junctions. *J. Phys. Chem. Lett.* **2014**, *5*, 205−207.

(45) Zhou, Y. H.; Fuentes-Hernandez, C.; Shim, J.; Meyer, J.; Giordano, A. J.; Li, H.; Winget, P.; Papadopoulos, T.; Cheun, H.; Kim, J.; Fenoll, M.; Dindar, A.; Haske, W.; Najafabadi, E.; Khan, T. M.; Sojoudi, H.; Barlow, S.; Graham, S.; Bredas, J. L.; Marder, S. R.; Kahn, A.; Kippelen, B. A Universal Method to Produce Low-Work Function Electrodes for Organic Electronics. *Science* **2012**, *336*, 327−332.

(46) Lee, B. R.; Lee, S.; Park, J. H.; Jung, E. D.; Yu, J. C.; Nam, Y. S.; Heo, J.; Kim, J. Y.; Kim, B. S.; Song, M. H. Amine-Based Interfacial Molecules for Inverted Polymer-Based Optoelectronic Devices. *Adv. Mater.* **2015**, *27*, 3553−3559.

(47) Torasso, N.; Armaleo, J. M.; Tagliazucchi, M.; Williams, F. J. Simplified Approach to Work Function Modulation in Polyelectrolyte Multilayers. *Langmuir* **2017**, *33*, 2169−2176.